Journal of the Mechanics and Physics of Solids 135 (2020) 103810

Contents lists available at ScienceDirect

Journal of the Mechanics and Physics of Solids

journal homepage: www.elsevier.com/locate/jmps

A phase field framework for dynamic adiabatic shear banding

Yun Xu[a], Pingbing Ming[b,c], Jun Chen[a,d,*]

[a] Laboratory of Computational Physics, Institute of Applied Physics and Computational Mathematics, Beijing 100088, PR China
[b] The State Key Laboratory of Scientific and Engineering Computing, Academy of Mathematics and Systems Science, Chinese Academy of Sciences, Beijing 100190, PR China
[c] School of Mathematical Sciences, University of Chinese Academy of Sciences, Beijing 100049, PR China
[d] Center for Applied Physics and Technology, Peking University, Beijing 100871, PR China

ARTICLE INFO

Article history:
Received 18 June 2019
Revised 26 November 2019
Accepted 27 November 2019
Available online 3 December 2019

Keywords:
Phase field
Variational formulation
Adiabatic shear bands
Strain gradient theory
Finite element simulation

ABSTRACT

We present a general variational formulation of phase field framework for dynamic adiabatic shear banding (ASBing). The ASB surface energy is derived from the Griffith's regularized ASB surface function, and the concept of shear banding energy density that characterized by the energy jump contour integral. We reveal that the ASB phase field formulation reduces to a standard strain-gradient plasticity model by energy minimization and ASB canonical analysis, which indicates that strain-gradient regularization for problems involving strain softening has been incorporated reasonably. The phase-field and plasticity coupled constitutive relations are developed within an atomistic potentials consistent hyperelastic-plasticity framework. The degraded volumetric strain energy governs the elastic responses, while the degraded deviatoric strain energy, as well as the ASB surface energy, accounts for the combined effects of shear localization, plasticity and fracture, which directly relates energy dissipation to the evolution of dynamic ASBs. Numerical simulations demonstrate the ability of this predictive ASB phase field framework in capturing discontinuous surfaces, and the removal of pathological mesh-dependence.

1. Introduction

Adiabatic shear banding (ASBing) is an important material failure mechanism preceding fracture. It is generally viewed as a dynamic behaviour that is triggered by strain softening, at the onset of which the homogeneous deformation abruptly localizes into a very narrow band (Bai and Dodd, 1992; Wright, 2002; Zener and Hollomon, 1944). The underlying physics of ASB is rather complex and still remains unclear.

Recently, the phase-field models are extensively used in fracture simulations for their capabilities of capturing complex crack propagations (Ambati et al., 2015; Duda et al., 2015; Giambanco and Ribolla, 2019; Loew et al., 2019; Martinez-Paneda et al., 2018; Tanne et al., 2018). Based on a regularized Griffith type formulation and the Γ- convergence theory (Francfort and Marigo, 1998), the crack discontinuities are smeared within a continuum phase-field approach, with an assumption that the damage energy is quadratic dependence upon the gradient of the damage.

A unified phase-field model for shear banding and fracture is presented for studying metal failure (Arriaga and Waisman, 2017; McAuliffe and Waisman, 2015). Based on a 'two-surface' formulation, Miehe (2011), Miehe et al. (2016),

* Corresponding author.
E-mail addresses: xu_yun@iapcm.ac.cn (Y. Xu), jun_chen@iapcm.ac.cn (J. Chen).

https://doi.org/10.1016/j.jmps.2019.103810
0022-5096/

Brepols et al. (2017) proposed gradient-extended damage-plasticity models for dynamic cracking. They introduce two independent internal variables and hence two separate yield surfaces of damage and plasticity for regularizing the crack discontinuity and the plastic response respectively. To decrease model complexion of gradient-extended damage-plasticity models, we aim to build a phase field framework that incorporates gradient-plasticity effects implicitly. It is developed for ASBing, and reduces to a standard strain-gradient plasticity model via energy minimization. To some degree this phase field framework is a plasticity model.

Our primary goal is to develop a general variational formulation of a phase field framework for simulating dynamic ASBing in elastic-plastic solids. The main idea consists four parts: a phase field formulation for ASBing, its relation to strain-gradient theory, a phase field and plasticity coupled constitutive model and numerical simulations. We explain them in the following several paragraphs. First, based on Griffith's theory, the ASB surface energy is constructed as the integral of the shear banding energy density over ASB surfaces. The shear banding energy density is taken to be the contour integral of the energy jump across ASB surfaces (Xu and Chen, 2015). The regularized surface energy of ASB, together with the degraded elastic energy, constitute the phase field energy in a general variational formulation.

Second, we prove that the phase field formulation of ASB reduces to a standard strain-gradient plasticity model, using energy minimization and the canonical structural analysis of ASB. This relationship deepens the understanding of ASB physical mechanisms including energy dissipation, shear instability and size effects. Meanwhile, it indicates that strain-gradient regularization for strain softening has been incorporated reasonably in this phase field formulation, which partly explains the mesh-independence in the numerical simulations.

Third, the phase-field and plasticity coupled constitutive relations are developed within a hyperelastic-plastic framework that is consistent with atomistic potentials (Xu et al., 2014). The degraded volumetric strain energy governs the elastic responses, while the degraded deviatoric strain energy, as well as the ASB surface energy, accounts for the combined effects of dynamic localization, plasticity and fracture, which directly relates energy dissipation to the evolution of dynamic ASBs.

Finally, numerical simulations demonstrate the capability of this predictive phase field model. Two tests of plane tension are carried out to show that the strain-softening responses in dynamic localization can be captured without pathological mesh-dependence. The advantage of this phase field formulation in capturing discontinuous surfaces is displayed by the study of collapsing thick-walled cylinders. The distribution and evolution of the multiple ASBs are in good agreement with experimental evidences.

The remainder of this paper is organized as follows. We develop the phase field framework of ASB in §2, including the construction of the shear banding energy density and ASB surface energy. It reduces to a strain-gradient plasticity model by energy minimization. The phase field and plasticity coupled constitutive model are presented in §3. System energy decomposition, constitutive equations derivation and finite element implementation are illustrated within the hyperelastic-plasticity consistent with atomistic potentials. Numerical simulations are provided in §4, and §5 summaries this paper.

2. ASB Phase field framework

Considering that ASBs fulfill three foundational ingredients of the Griffith theory: discontinuity, propagating with a threshold energy and irreversibility, let $\Gamma \subset \Omega$ be the discontinuous ASB surfaces, the surface energy of ASB can be defined as

$$\Gamma_A = \int_\Gamma \mathcal{G}_A d\,\Gamma, \tag{1}$$

where $\mathcal{G}_A$ is the shear banding energy density. From experimental investigations, $\mathcal{G}_A$ can be illustrated as the shear-band dissipation energy or shear-band toughness (Grady, 1994), and the ASB energy failure criterion (Dolinski and Rittel, 2015; Dolinski et al., 2010). We will explain the construction of $\mathcal{G}_A$ in the following subsection.

The dynamic behaviours of ASB are governed by minimizing the following free energy functional

$$\Psi = \int_\Omega \Psi^e(\mathbf{E})\, d\mathbf{x} + \int_\Gamma \mathcal{G}_A d\,\Gamma, \tag{2}$$

where $\Psi^e(\mathbf{E}) = \frac{1}{2}\mathbf{E} : \mathbb{C} : \mathbf{E}$ is the elastic strain energy density (Bourdin et al., 2000; Francfort and Marigo, 1998), with $\mathbb{C}$ the Lagrangian tangent modulus and $\mathbf{E}$ the Green-Lagrangian strain tensor. They are listed in the notation table.

Notation	Description	Dimension
$\mathbb{C}$	Lagrangian tangent modulus	4th-order tensor
$\mathbf{E}$	Green-Lagrangian strain	2nd-order tensor
$\Gamma \subset \Omega$	ASB surface	
$\mathcal{G}_A$	shear banding energy density	scalar
Ψ	free energy	scalar
$\boldsymbol{\sigma}$	Cauchy stress	2nd-order tensor

(*continued on next page*)

Notation	Description	Dimension
$[\cdot]$	jump across ASB surface	
$\mathbf{n}$	current normal vector	vector
$\mathbf{P}$	first Piola-Kirchhoff stress	2nd-order tensor
G_B	energy density as integral over Γ_B	scalar
$\mathbf{N}$	reference normal vector	vector
ϕ	phase field variable	scalar
ℓ	phase field length scale	scalar
Q	microstresses in gradient plasticity	scalar
τ_i	moment stresses in gradient plasticity	vector
$\mathbf{\Sigma} = (Q, \ell^{-1}\tau_i)$	enhanced effective stress	
$\Sigma = \lvert\mathbf{\Sigma}\rvert$	magnitude of $\mathbf{\Sigma}$	scalar
$\dot{\varepsilon}_p$	equivalent plastic strain rate	scalar
$\dot{\varepsilon}_{p,i}$	spatial gradient of $\dot{\varepsilon}_p$	vector
$\dot{\mathbf{E}}_p = (\dot{\varepsilon}_p, \ell\dot{\varepsilon}_{p,i})$	gradient enhanced plastic strain rate	
$\dot{E}_p = \lvert\dot{\mathbf{E}}_p\rvert$	magnitude of $\dot{\mathbf{E}}_p$	scalar
$\mathbf{F} = \mathbf{F}^e\mathbf{F}^p$	multiplicative decomposition	2nd-order tensor
$\mathbf{C} = \mathbf{F}^T\mathbf{F}$	Cauchy-Green deformation tensor	2nd-order tensor

2.1. Shear banding energy density

The shear banding energy density represents the energy required for an unit area extension of an ASB. It relates the advancement of ASBs to the competition between the surface energy and material resistance. We derive the shear banding energy density from the contour integral around the band tip (Xu and Chen, 2015).

Let Ω_0 and Ω be open sets in $\mathbb{R}^N$, the deformation

$$\mathbf{X} \mapsto \mathbf{x} = \varphi(\mathbf{X}, t), \quad \forall \mathbf{X} \in \Omega_0, \quad t \geq 0 \tag{3}$$

maps the initial position $\mathbf{X}$ to current coordinate $\mathbf{x}$. The deformation gradient and its determinant or Jacobian are defined by

$$\mathbf{F} = \nabla_{\mathbf{X}}\varphi, \quad F_{iK} = \frac{\partial \varphi_i}{\partial X_K} = \frac{\partial x_i}{\partial X_K}, \quad J = \det(\mathbf{F}).$$

The governing equations are the conservation law of mass, momentum and energy:

$$\begin{cases} \rho J = \rho_0 \\ \rho\ddot{\mathbf{u}} = \rho\mathbf{b} + \nabla_x \cdot \boldsymbol{\sigma} \\ \rho\dot{\epsilon} = \rho r + (\nabla_x \mathbf{v}) : \boldsymbol{\sigma} + \nabla_x \mathbf{q}, \end{cases} \tag{4}$$

where $\dot{\mathbf{u}}$, $\dot{\mathbf{v}}$ and $\dot{\epsilon}$ indicate the material time derivatives. (∇_x), $(\nabla_x \cdot\ )$ are the gradient and divergence operators in the current configuration. $\mathbf{u} = \mathbf{x} - \mathbf{X}$ denotes the displacement vector, ρ_0 and ρ are the initial and current density. While $\dot{\mathbf{u}} = \mathbf{v}$, $\boldsymbol{\sigma}$, ϵ and q are velocity, Cauchy stress tensor, specific energy and heat flux, respectively. Based on the conservation law, the energy jump across an ASB surface Γ can be expressed as (Olmstead, 1994; Wright and Walter, 1996):

$$[\dot{S}] = (\boldsymbol{\sigma}\mathbf{n}) \cdot [\mathbf{v}] - [\mathbf{q} \cdot \mathbf{n}], \tag{5}$$

where $[\,]$ denotes the jump across Γ, the signs for matrix-matrix and matrix-vector multiplications are omitted, and the notation ' $\cdot$ ' is used for scalar product. Note that $\mathbf{n}$ is the current unit vector normal to Γ, and $(\boldsymbol{\sigma}\mathbf{n}) \cdot [\mathbf{v}]$ is a scalar. In the following relationships

$$\dot{\Psi} = (\boldsymbol{\sigma}\mathbf{n}) \cdot \mathbf{v}, \quad \mathbf{q} \cdot \mathbf{n} = \dot{\mathbf{F}}^T : \mathbf{P}, \tag{6}$$

$\dot{\Psi}$ is the stress work rate, and $\mathbf{P}$ is the first Piola-Kirchhoff stress with $\mathbf{P} = \frac{\partial \Psi}{\partial \mathbf{F}}$. The jump of the redundant stress work $[S]$ can be transformed into

$$[S] = [\Psi] - [\mathbf{F}^T : \mathbf{P}]. \tag{7}$$

It is found that Eq. (7) can be related to the Eshelby energy-momentum tensor $\mathbf{S}$ by expanding the scalar $[S]$ to its matrix form as

$$\mathbf{S} = \Psi\mathbf{I} - \mathbf{F}^T\mathbf{P}. \tag{8}$$

The energy density of an ASB surface (as shown in Fig. 1(A)) can be calculated from the integral of $\mathbf{S}$ over a contour Γ_B (as shown in Fig. 1(B)):

$$G_B = \hat{\mathbf{e}} \cdot \int_{\Gamma_B} \mathbf{S}\mathbf{N} d\,\Gamma_B = \hat{\mathbf{e}} \cdot \int_{\Gamma_B} \left(\Psi\mathbf{N} - \mathbf{F}^T\mathbf{P}\mathbf{N}\right) d\,\Gamma_B, \tag{9}$$

where $\mathbf{N}$ denotes the reference unit vector normal to Γ_B, and $\hat{\mathbf{e}}$ is the unit vector along the ASB propagation direction. Generally, this contour integral G_B is path-dependent in elastic-plastic solids under dynamic loading condition, and should be obtained by correcting the far-field integral G_{far} (as shown in Fig. 1(C)) (Xu and Chen, 2015). When G_B reaches a critical value that equals to the shear banding energy density, the ASBs start to initiation and propagation.

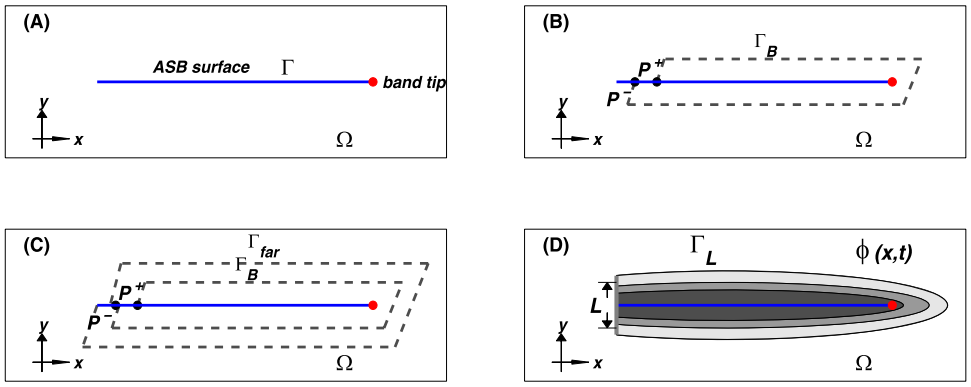

Fig. 1. Phase field approximation of an ASB surface. (A) The discontinuous ASB surface Γ in a solid Ω. (B) The contour integral path Γ_B around the band tip. (C) The far field contour integral path Γ_{far}. (D) The phase field approximation of a regularized ASB surface, with $\phi(\mathbf{x}, t)$ varied from 0 to 1.

2.2. Surface energy of ASB

The shear banding energy density in Eq. (1) is assumed to be a material constant for computational simplicity, and the ASB surface energy can be written as

$$\Gamma_A = \mathcal{G}_A \int_\Gamma d\,\Gamma. \tag{10}$$

The regularization formulation of Eq. (2) is derived as (Bourdin et al., 2000)

$$\Psi_\ell(\phi) = \int_\Omega g(\phi)\Psi^e(\mathbf{E})\,d\mathbf{x} + \mathcal{G}_A \int_\Omega \Big(\frac{1}{2\ell}\phi^2 + \frac{\ell}{2}|\nabla\phi|^2\Big)\,d\mathbf{x}, \tag{11}$$

with the degradation function

$$g(\phi) = (1-\phi)^2 + \eta. \tag{12}$$

The variable ϕ is defined as

$$\phi(\mathbf{x}) = \begin{cases} 1 & \mathbf{x} \subseteq \Gamma \\ 0 & \mathbf{x} \nsubseteq \Gamma, \end{cases} \tag{13}$$

where the length scale ℓ denotes the width of the smearing ASB (as illustrated in Fig. 1(D)). The small constant η is introduced to avoid possible numerical difficulties in the case of $\phi = 1$. The regularized energy of Eq. (11) approximates Eq. (2) for the Γ- convergence with $\ell \to 0$.

Let

$$\gamma(\phi, \nabla\phi) = \frac{1}{2\ell}\phi^2 + \frac{\ell}{2}|\nabla\phi|^2 \tag{14}$$

be the ASB surface density function in Eq. (11). The ASB surface energy Γ_A can then be regularized as

$$\Gamma_A(\ell, \phi) = \mathcal{G}_A \int_\Omega \gamma(\phi, \nabla\phi)\,d\mathbf{x}, \tag{15}$$

with the following integration function of the ASB surface

$$\Gamma_\ell(\phi) = \int_\Omega \gamma(\phi, \nabla\phi)\,d\mathbf{x}. \tag{16}$$

Note that $\gamma(\phi, \nabla\phi)$ is the same as that defined for cracks (Miehe, 2011), and similarly, the Euler equation of the variational functional

$$\phi = \mathrm{Arg}\{\inf \Gamma_A(\ell, \phi)\} \tag{17}$$

is the Ginzburg-Landau type differential equation

$$\phi(\mathbf{x}) - \ell^2 \triangle\phi(\mathbf{x}) = 0. \tag{18}$$

Considering that ASBs are essentially 1-d structures as mentioned in Wright and Ravichandran (1997), the solution of Eq. (18) can be expressed by the following exponential function

$$\phi(\mathbf{x}) = e^{-\frac{|\mathbf{x}|}{\ell}}, \tag{19}$$

which coincides with the approximation of the basic phase field variable. The minimized ASB surface energy can be obtained with Eq. (19).

2.3. Reduces to strain-gradient plasticity

It is worth noting that within the infinitesimal strain theory, the above ASB phase field framework reduces to a standard strain-gradient plasticity model using energy minimization. In ASB canonical analysis, the shear band was considered as essentially a 1-d structure (Wright and Ravichandran, 1997). Only the $x-$component velocity v and the $xY-$component strain $\varepsilon = u_y$ are nonzero (Glimm et al., 1993). The shear strain ε is decomposed into elastic and plastic parts

$$\varepsilon = \varepsilon_e + \varepsilon_p. \tag{20}$$

The elastic strain energy density is given by

$$\Psi^e(\varepsilon) = \frac{1}{2}\mu(\varepsilon - \varepsilon_p)(\varepsilon - \varepsilon_p), \tag{21}$$

with the shear stress

$$\sigma = \mu(\varepsilon - \varepsilon_p), \tag{22}$$

where μ being the shear modulus. Inserting $\dot{\varepsilon} = v_y$ into the rate form of the shear stress

$$\dot{\sigma} = \mu(\dot{\varepsilon} - \dot{\varepsilon}_p), \tag{23}$$

one get

$$\dot{\sigma}/\mu = v_y - \dot{\varepsilon}_p. \tag{24}$$

Glimm et al. (1993) address that

$$v_y = \dot{\varepsilon}_p, \tag{25}$$

since $1/\mu$ is moderately small. Meanwhile, v_y is approximated as (Eq. (16) in Wright and Ravichandran (1997)):

$$v_y = \zeta e^{-\frac{z}{m_c}}, \tag{26}$$

where ζ is the strain rate at the band center, and m_c is a small constant that relates to the width of the shear band (Wright and Ravichandran, 1997). Combining Eqs. (25) and (26),

$$\dot{\varepsilon}_p(z) = \zeta e^{-\frac{z}{m_c}}. \tag{27}$$

Considering that m_c is a regularization parameter, Eq. (27) can be rewritten as

$$\dot{\varepsilon}_p(x) = \zeta e^{-\frac{|x|}{\ell}}, \tag{28}$$

where $\ell = m_c$ and $x = 0$ denotes the band center. Using the formula for the phase field variable $\phi(x)$,

$$\dot{\varepsilon}_p(x) = \zeta\phi(x). \tag{29}$$

Substitute Eq. (29) into Eq. (14) yields

$$\gamma(\dot{\varepsilon}_p, \dot{\varepsilon}_{p,i}) = \frac{1}{\zeta^2}\left(\frac{1}{2\ell}\dot{\varepsilon}_p^2 + \frac{\ell}{2}\dot{\varepsilon}_{p,i}\dot{\varepsilon}_{p,i}\right), \tag{30}$$

and the following integration function of the ASB surface

$$\Gamma_\ell(\dot{\varepsilon}_p, \dot{\varepsilon}_{p,i}) = \int_\Omega \gamma(\dot{\varepsilon}_p, \dot{\varepsilon}_{p,i})\, d\Omega. \tag{31}$$

The equivalent plastic strain ε_p and its spatial gradient $\varepsilon_{p,i}$ can be calculated from

$$\varepsilon_p = \int \dot{\varepsilon}_p\, dt, \quad \varepsilon_{p,i} = \int \dot{\varepsilon}_{p,i}\, dt. \tag{32}$$

It may be interesting by rescaling γ as

$$\tilde{\gamma} = \zeta\sqrt{2\ell}\sqrt{\gamma} = \sqrt{\dot{\varepsilon}_p^2 + \ell^2\dot{\varepsilon}_{p,i}\dot{\varepsilon}_{p,i}}, \tag{33}$$

and $\tilde{\gamma}$ turned out to be the gradient enhanced plastic strain rate $\dot{E}_p$ that is defined in most strain gradient theories (Fleck and Hutchinson, 2001; Gudmundson, 2004; Hutchinson, 2012):

$$\dot{E}_p = \sqrt{\dot{\varepsilon}_p^2 + \ell^2\dot{\varepsilon}_{p,i}\dot{\varepsilon}_{p,i}}. \tag{34}$$

$$\tilde{\gamma} = \dot{E}_p, \quad \gamma = \frac{1}{2\ell\zeta^2}\dot{E}_p^2. \tag{35}$$

This relationship between the phase field formulation and the strain gradient theory can deepen the understandings of ASB, including energy dissipation, strain softening and size effects.

The total energy of Eq. (11) can be expressed as

$$\Psi_\ell(\phi) \triangleq \Psi^e_{PF} + \Psi^p_{PF}, \tag{36}$$

with

$$\Psi^e_{PF} = \int_\Omega g(\phi)\Psi^e(\boldsymbol{\varepsilon})\, d\mathbf{x}, \quad \Psi^p_{PF} = \mathcal{G}_A \int_\Omega \Big(\frac{1}{2\ell}\phi^2 + \frac{\ell}{2}|\nabla\phi|^2\Big)\, d\mathbf{x}. \tag{37}$$

The stress quantities that are work conjugate to the strain quantities (Fleck and Hutchinson, 2001; Hutchinson, 2012):

$$\begin{aligned}\dot{\Psi}_\ell(\varepsilon^e_{ij}, \varepsilon_p, \varepsilon_{p,i}) &= \frac{\partial \Psi^e_{PF}}{\partial \varepsilon^e_{ij}}\dot{\varepsilon}^e_{ij} + \frac{\partial \Psi^p_{PF}}{\partial \varepsilon_p}\dot{\varepsilon}_p + \frac{\partial \Psi^p_{PF}}{\partial \varepsilon_{p,i}}\dot{\varepsilon}_{p,i} \\ &= \sigma_{ij}\dot{\varepsilon}^e_{ij} + Q\dot{\varepsilon}_p + \tau_i\dot{\varepsilon}_{p,i}.\end{aligned} \tag{38}$$

Let $\boldsymbol{\Sigma} = (Q, \ell^{-1}\tau_i)$ denotes the enhanced effective stress pair consists of the microstresses Q and the moment stresses τ_i. They work conjugate to the strain quantities $\dot{\varepsilon}_p$ and $\dot{\varepsilon}_{p,i}$, respectively. The gradient enhanced plastic strain rate can be written in the pair form as $\dot{\mathbf{E}}_p = (\dot{\varepsilon}_p, \ell\dot{\varepsilon}_{p,i})$. The inner product of $\boldsymbol{\Sigma}\cdot\dot{\mathbf{E}}_p$ yields a scalar as

$$\begin{aligned}&\boldsymbol{\Sigma}\cdot\dot{\mathbf{E}}_p = Q\dot{\varepsilon}_p + \tau_i\dot{\varepsilon}_{p,i}, \\ &\Sigma = |\boldsymbol{\Sigma}| = \sqrt{Q^2 + \ell^{-2}\tau_i\tau_i}, \\ &\dot{E}_p = |\dot{\mathbf{E}}_p| = \sqrt{\dot{\varepsilon}_p^2 + \ell^2\dot{\varepsilon}_{p,i}\dot{\varepsilon}_{p,i}}.\end{aligned} \tag{39}$$

The minimized ASB surface energy $\Gamma_A(\ell, \dot{\varepsilon}_p, \dot{\varepsilon}_{p,i})$ can be calculated from Eq. (15) as

$$\Gamma_A(\ell, \dot{\varepsilon}_p, \dot{\varepsilon}_{p,i}) = \mathcal{G}_A \int_\Omega \gamma(\dot{\varepsilon}_p, \dot{\varepsilon}_{p,i})\, d\mathbf{x}, \tag{40}$$

which relates energy dissipation to the evolution of ASB surface. Substituting Eq. (35) in Eq. (40):

$$\begin{aligned}\Gamma_A(\ell, \dot{\varepsilon}_p, \dot{\varepsilon}_{p,i}) &= \int_\Omega \frac{\mathcal{G}_A}{2\ell\zeta^2}\dot{E}_p^2\, d\mathbf{x} \\ &= \int_\Omega h\dot{E}_p^2\, d\mathbf{x},\end{aligned} \tag{41}$$

where $h = \frac{\mathcal{G}_A}{2\ell\zeta^2}$ is the hardening modulus. Obviously, $\Gamma_A(\ell, \dot{\varepsilon}_p, \dot{\varepsilon}_{p,i}) \geq 0$ follows from $h > 0$, with $\ell > 0$, $\zeta > 0$. It provides a simple way to construct a scalar work-conjugate stress Σ in terms of $\dot{E}_p$ as

$$\Sigma = \frac{\mathcal{G}_A}{2\ell\zeta^2}\dot{E}_p, \tag{42}$$

and ensures that the plastic work rate is non-negative, i.e. $\boldsymbol{\Sigma}\cdot\dot{\mathbf{E}}_p \geq 0$. The free energy of Eq. (11) changes into

$$\Psi_\ell(\dot{\varepsilon}_p, \dot{\varepsilon}_{p,i}) = \int_\Omega g(\dot{\varepsilon}_p)\Psi^e(\boldsymbol{\varepsilon})\, d\mathbf{x} + \int_\Omega h\dot{E}_p^2\, d\mathbf{x}, \tag{43}$$

with the degradation function

$$g(\dot{\varepsilon}_p) = (1 - \frac{1}{\zeta}\dot{\varepsilon}_p)^2 + \eta. \tag{44}$$

Let $g(\dot{\varepsilon}_p) = 1$, the above Eq. (43) is simplified as

$$\Psi_\ell(\dot{\varepsilon}_p, \dot{\varepsilon}_{p,i}) = \int_\Omega \Psi^e(\boldsymbol{\varepsilon})\, d\mathbf{x} + \int_\Omega h\dot{E}_p^2\, d\mathbf{x}. \tag{45}$$

It equivalents to the minimum principle (Fleck and Hutchinson, 2001; Fleck and Willis, 2009), or the strain energy of strain gradient plasticity (Hutchinson, 2012). Finally, based on this energy formulation, the internal virtual work and the microstress equilibrium equation can be identified similar to standard strain gradient theories.

3. Constitutive model

3.1. System energy

The system Helmholtz energy density Ψ is obtained from the atomistic potential energy by Cauchy-Born rule (Born and Huang, 1954; E and Ming, 2007),

$$\Psi(\mathbf{r}^m, \beta) = E_{col}(\mathbf{r}^m) + E_{vib}(\mathbf{r}^m, \beta). \tag{46}$$

E_{col} is the cold energy of the system, and it is constructed from the embedded-atom method (EAM) potential function (Daw and Baskes, 1984),

$$E_{col} = \frac{1}{v_0}\sum_m \Big(U\big(f(\mathbf{r}^m)\big) + \frac{1}{2}\phi(\mathbf{r}^m)\Big). \tag{47}$$

In the above function, U is the embedding energy, $f(\mathbf{r}^m)$ is the density of the host at the position $\mathbf{r}^m$ but without atom m, ϕ is the short-range pair potential, and v_0 is the volume of the cell element. The cold energy is the sum of the individual contributions.

E_{vib} is the thermal vibration part of the system, and it is approximated by the local harmonic approximation (LeSar et al., 1989) (which is proved to be accurate up to half of the melting temperature):

$$E_{vib} = \sum_m \frac{1}{2\beta}\ln\frac{\|D(\{\mathbf{r}^m\})\|}{(2\pi/\beta)^3}, \tag{48}$$

where $\mathbf{r}^m$ denotes the atom positions, $\beta = 1/k_BT$, k_B is Boltzmann's constant and v_0 is a reference volume. The effects of atomic vibrate frequency have been included in the dynamic matrix $D(\{\mathbf{r}^m\})$, and $\|\cdot\|$ denotes the determinant of the matrix.

In the point view of Simo (1988), Ψ can be decomposed into the volumetric strain energy Ψ^e and the deviatoric strain energy Ψ^p to address the uncoupled volumetric deviatoric response:

$$\Psi = \Psi^e(\mathbf{F}) + \Psi^p(\mathbf{F}, \mathbf{F}^p). \tag{49}$$

The multiplicative decomposition $\mathbf{F} = \mathbf{F}^e\mathbf{F}^p$, $\mathbf{F^e} = J^{\frac{1}{3}}\mathbf{I}$, $\mathbf{F^p} = J^{-\frac{1}{3}}\mathbf{F}$, which satisfies $|\mathbf{F}^p| = \mathbf{1}$, $J = |\mathbf{F}| = |\mathbf{F}^e|$. The volumetric part is supposed to be stored in the elastic deformation, and is determined by the upscaled elastic Green's strain tensor and the underlying lattice structure. The deviatoric part is the outcome of atomic bonds breaking and dislocation motions. The Lagrangian tangent modulus $\mathbb{C}$ is

$$\mathbb{C} = \frac{\partial^2\bar{\Psi}(\mathbf{E})}{\partial\mathbf{E}\partial\mathbf{E}}, \tag{50}$$

where $\mathbf{E}$ is the Green-Lagrangian strain tensor

$$\mathbf{E} = \frac{1}{2}(\mathbf{C} - \mathbf{I}) = \frac{1}{2}(\mathbf{F}^T\mathbf{F} - \mathbf{I}), \tag{51}$$

and $\mathbf{C}$ is the right Cauchy-Green deformation tensor. The elastic Green-Lagrangian strain tensor $\mathbf{E}^e$ is defined as

$$\mathbf{E}^e = \frac{1}{2}(\mathbf{C}^e - \mathbf{I}) = \frac{1}{2}(\mathbf{F}^{e^T}\mathbf{F}^e - \mathbf{I}). \tag{52}$$

The volumetric strain energy Ψ^e can be calculated from $\mathbb{C}$ and $\mathbf{E}^e$ as

$$\Psi^e = \frac{1}{2}\mathbf{E}^e : \mathbb{C} : \mathbf{E}^e. \tag{53}$$

The deviatoric strain energy

$$\Psi^p = \bar{\Psi} - \Psi^e = (E_{col} + E_{vib}) - \Psi^e. \tag{54}$$

3.2. Coupled with phase field formulation

Dynamic shear bands accompanied by large deformation and finite strain, and the plasticity evolution that resulted from dislocation nucleation and multiplication plays an important role in the initiation of ASBs. We suggest that the deviatoric part energy Ψ^p in Eq. (49) be included into the total energy of Eq. (2) for characterizing shear localization before ASB initiation. It is constructed as

$$\Psi_\ell(\mathbf{F}, \mathbf{F}^p, \phi) = \int_\Omega g(\phi)\big(\Psi^e(\mathbf{F}) + \Psi^p(\mathbf{F}, \mathbf{F}^p)\big)\,d\mathbf{x} + \int_\Gamma \mathcal{G}_A d\,\Gamma. \tag{55}$$

The first term $g(\phi)\Psi^e(\mathbf{F})$ denotes the degraded volumetric strain energy density of the undamaged solid. The second term $g(\phi)\Psi^p(\mathbf{F}, \mathbf{F}^p)$ denotes the degraded deviatoric strain energy density of the plasticity-damage coupled solid, and the third term denotes the ASB surface energy. The degraded plasticity-damage energy is defined as

$$\Psi_{\ell,p}(\mathbf{F}, \mathbf{F}^p, \phi) = \int_\Omega g(\phi)\Psi^p(\mathbf{F}, \mathbf{F}^p)\,d\mathbf{x} + \int_\Gamma \mathcal{G}_A d\,\Gamma. \tag{56}$$

The Cauchy stress can be computed as

$$\begin{aligned}\boldsymbol{\sigma} &= g(\phi)J^{-1}\mathbf{F^e}\mathbf{S}\mathbf{F}^{e^T}\\ &= g(\phi)J^{-1}\mathbf{F^e}\frac{\partial\Psi^e}{\partial\mathbf{E}^e}\mathbf{F}^{e^T}\\ &= g(\phi)J^{-\frac{1}{3}}\mathbb{C} : \mathbf{E}^e.\end{aligned} \tag{57}$$

The associative flow rule can be derived based on the plasticity-damage energy and the principle of maximum plastic dissipation. Introduce the plasticity-damage functional $\boldsymbol{\varphi}(\mathbf{b}^e)$

$$\boldsymbol{\varphi}(\mathbf{b}^e) = \frac{\partial \Psi_{\ell,p}(\mathbf{F}, \mathbf{F}^p, \phi)}{\partial \mathbf{g}} = \frac{\partial \Psi_{\ell,p}(\mathbf{g}, \mathbf{b}^{e^{-1}}, \mathbf{F}, \phi)}{\partial \mathbf{g}}, \tag{58}$$

where $\mathbf{b}^e = \mathbf{F}^e \mathbf{F}^{e^T}$. The unit tensor in the intermediate configuration is denoted by $\mathbf{g}$, with its Lie derivative defined as

$$\mathbf{L_v g} = \mathbf{F}^T \mathbf{g} \mathbf{F} = \bar{\mathbf{C}}, \tag{59}$$

in which the overbar denotes the intermediate configuration. The numerical strategy for computing $\boldsymbol{\varphi}(\mathbf{b}^e)$ is to find the inverse matrix of $\mathbf{g}$ (denoted as $\tilde{\mathbf{g}}$) and

$$\boldsymbol{\varphi}(\mathbf{b}^e) = \frac{\partial \Psi_{\ell,p}}{\partial \mathbf{g}} = \Psi_{\ell,p} \tilde{\mathbf{g}}, \tag{60}$$

in which $\boldsymbol{\varphi}(\mathbf{b}^e)$ is a nonzero tensor functional. The Kirchhoff stress $\boldsymbol{\tau}$ can be calculated as (Simo, 1988; Simo and Hughes, 1998):

$$\boldsymbol{\tau} = Jp\mathbf{g} + 2J^{-2/3}\mathrm{dev}[\boldsymbol{\varphi}(\mathbf{b}^e)], \tag{61}$$

where $p = d(g(\phi)\Psi^e)/dJ$ is the hydrostatic pressure. The maximum plastic dissipation implies the following plasticity-damage evolution equation (the detailed proof is given in Xu et al. (2014)):

$$\frac{\partial}{\partial t}\varphi(\mathbf{C}^{p^{-1}}) = -\frac{2}{3}\delta \mathrm{tr}[\boldsymbol{\varphi}(\mathbf{b}^e)]\mathbf{r}, \tag{62}$$

where δ is the consistency parameter, $\mathbf{C}^p = \mathbf{F}^{p^T}\mathbf{F}^p$, and

$$\dot{\boldsymbol{\varepsilon}}_p = \sqrt{\frac{2}{3}}\delta. \tag{63}$$

The plastic flow direction $\mathbf{r}$ is calculated as

$$\mathbf{r} = \mathrm{dev}[\boldsymbol{\tau}]/\|\mathrm{dev}[\boldsymbol{\tau}]\|, \quad \|\mathrm{dev}[\boldsymbol{\tau}]\| = \Big(\frac{3}{2}\mathrm{dev}[\boldsymbol{\tau}] : \mathrm{dev}[\boldsymbol{\tau}]\Big)^{\frac{1}{2}}. \tag{64}$$

The associative flow rule is explained in Remark 3.1.

Remark 3.1. Consider a specific example by taking $\boldsymbol{\varphi}(\mathbf{b}^e) = \mu g(\phi)\mathbf{b}^e$, where μ is the shear modulus, the above Eq. (62) leads to the following evolution equation of plastic flow rule:

$$\frac{\partial}{\partial t}(\bar{\mathbf{C}}^{p^{-1}}) = -\frac{2}{3}\delta g(\phi)[\mathbf{C}^{p^{-1}} : \mathbf{C}]\mathbf{F}^{-1}\mathbf{r}\mathbf{F}^{-T}. \tag{65}$$

Let $g(\phi) = 1$ for simplicity, Eq. (65) is the same as that in Simo and Hughes (1998) (p.312), and the free energy reads as:

$$\begin{aligned} U(J^e) &= \tfrac{1}{2}\kappa\left(\tfrac{1}{2}(J^{e^2} - 1) - \log J^e\right) \\ \bar{W}(\bar{\mathbf{b}}^e) &= \tfrac{1}{2}\mu(\mathrm{tr}[\bar{\mathbf{b}}^e] - 3), \end{aligned} \tag{66}$$

which is the widely used Neo-Hookean model. It indicates for the choice of a linear functional $\boldsymbol{\varphi}(\mathbf{b}^e)$, the coupled phase field model may relate to the degraded Neo-Hookean model.

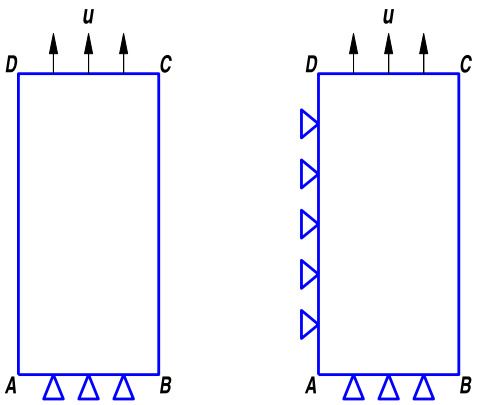

Fig. 2. Loading conditions of rectangular plane strain model. Left: Tension test I; Right: Tension test II.

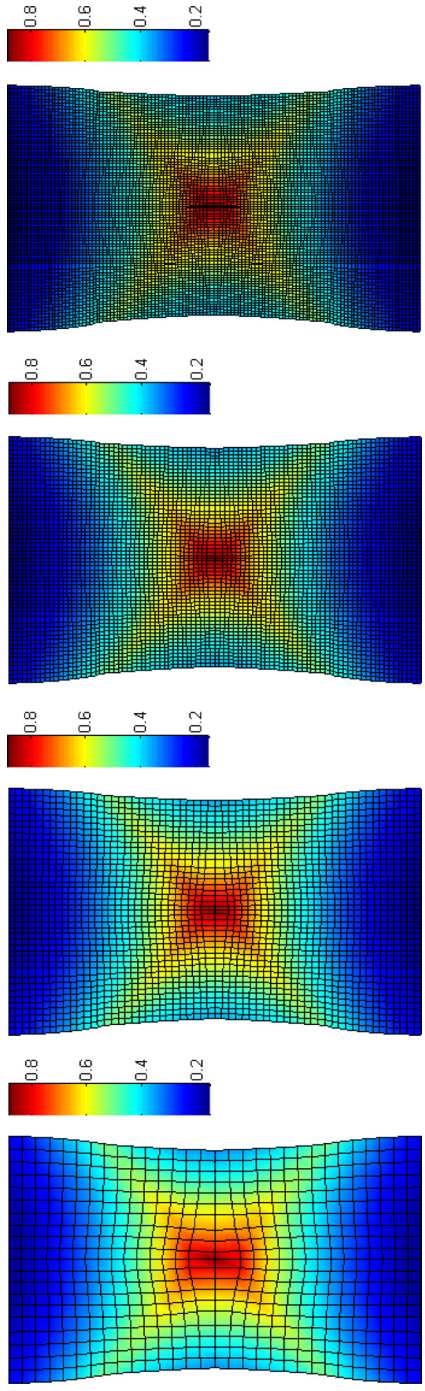

Fig. 3. Contours of equivalent plastic strain under plane strain tension I on four different meshes (from left to right). The length parameter is fixed at $\ell = 0.5$ mm.

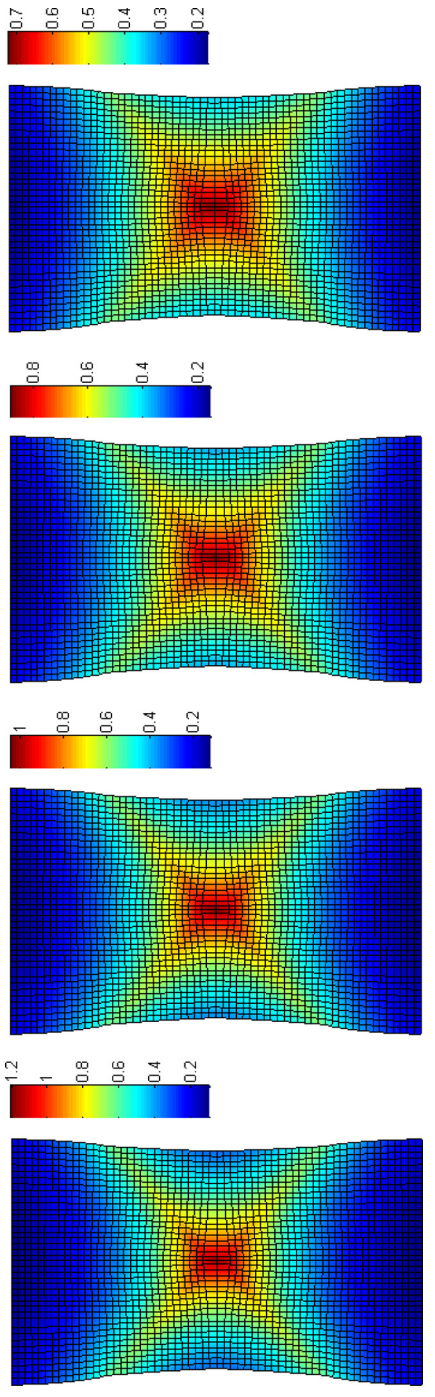

Fig. 4. Contours of equivalent plastic strain under plane strain tension I with four different values of the length parameter $\ell = 0.3$ mm, $\ell = 0.4$ mm, $\ell = 0.5$ mm and $\ell = 0.6$ mm on a fixed mesh (from left to right).

The variation of Eq. (55) with respect to $\delta\phi$ renders the weak form of the phase field contribution,

$$\int_\Omega \Big(-2(1-\phi)\delta\phi\big(\Psi^e+\Psi^p\big)+\mathcal{G}_A\big(\frac{1}{\ell}\phi\delta\phi+\ell\nabla\phi\cdot\nabla\delta\phi\big)\Big)\,d\mathbf{x}=0, \tag{67}$$

and the phase field equilibrium equation

$$\mathcal{G}_A\big(\frac{1}{\ell}\phi-\ell\triangle\phi\big)-2(1-\phi)(\Psi^e+\Psi^p)=0. \tag{68}$$

The full set of constitutive equations can be obtained with Eqs. (4), (57) and (62).

3.3. Finite element implementation

Updated Lagrangian finite element scheme is used in this simulation. The finite interpolations of displacement and velocity are

$$u_i(\mathbf{X},t)=u_{iI}(t)N_I(\mathbf{X}),\quad v_i(\mathbf{X},t)=v_{iI}(t)N_I(\mathbf{X}). \tag{69}$$

The momentum conservation equation can be written as:

$$\int_\Omega N_I\rho\dot{v}_i d\Omega+\int_\Omega\frac{\partial N_I}{\partial x_j}\sigma_{ji}d\Omega-\int_{\Gamma_t}N_I\bar{t}_i d\Gamma=0, \tag{70}$$

where $\bar{t}_i$ is the loading force on boundary Γ_t. Let $f_{iI}^{int}=\int_\Omega\frac{\partial N_I}{\partial x_j}\sigma_{ji}d\Omega$, $f_{iI}^{ext}=\int_{\Gamma_t}N_I\bar{t}_i d\Gamma$, the discrete momentum equation is transformed into:

$$M_{iJIJ}\dot{v}_{JJ}=f_{iI}^{ext}-f_{iI}^{int}, \tag{71}$$

where $M_{iJIJ}=\delta_{ij}\int_\Omega\rho N_I N_J d\Omega$ is the mass matrix. It is solved by the second-order explicit time integration algorithm. For 2-d computation, the isoparametric 4-node element on quadrilateral mesh with 2×2 Gauss quadrature scheme is used. Since the computation is carried out over Gauss quadrature points, the stress and strain at finite element nodes are recovered from the shape functions.

Mesh failure technique is adopted in finite element method based on the energy release rate criterion. Once the node is judged to be failure, it will be split into two new nodes, with velocities set to be one half of that of the failure node at current time. The crack propagates along the common side of two adjacent elements rather than crossing the interior of an element by simplicity assumption. The crack will grow if $G=\Gamma$, where $\Gamma=1.09\times10^4\mathrm{J}\cdot\mathrm{m}^{-2}$ is the fracture energy per unit area. ASBs initiate at the shear banding energy density $\mathcal{G}_A=2.15\times10^3\mathrm{J}\cdot\mathrm{m}^{-2}$, which is much smaller than that of the crack initiation. The value of $\mathcal{G}_A$ is taken to be $2.36\times10^3\mathrm{J}\cdot\mathrm{m}^{-2}$ for steel (Zhou et al., 1998).

4. Numerical study

The computational framework of the phase field formulation is applied to simulate the evolution of ASBs under strain softening conditions. First, a rectangular specimen is loaded under different tensions (Anand et al., 2012; McAuliffe, 2014; Tvergaard and Needleman, 1995). The material of this specimen is taken to be the stainless steel SS304L. The following tension test I and tension test II are different only in boundary conditions. The specimen size is 20 mm × 30 mm, and the computation is carried out under 2-d plane-strain conditions. We want to test two problems: (i) mesh dependency,

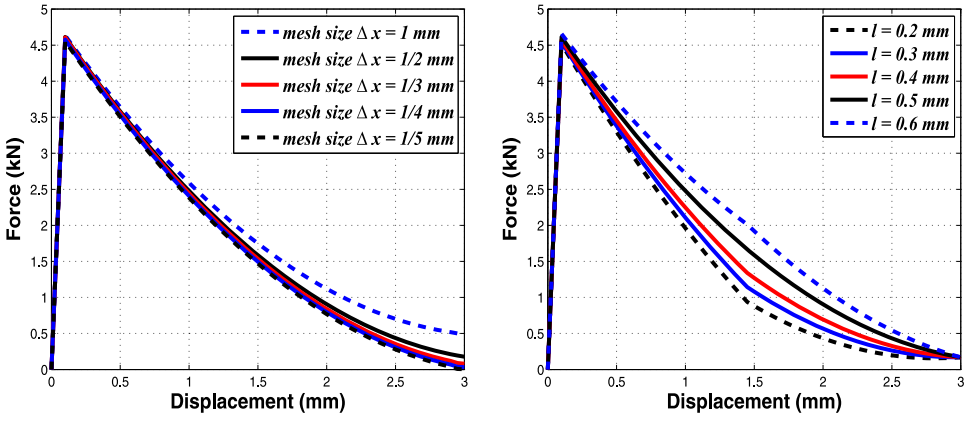

Fig. 5. Force versus displacement curves under plane strain tension I. Left: for different computational mesh sizes; Right: for different ℓ values.

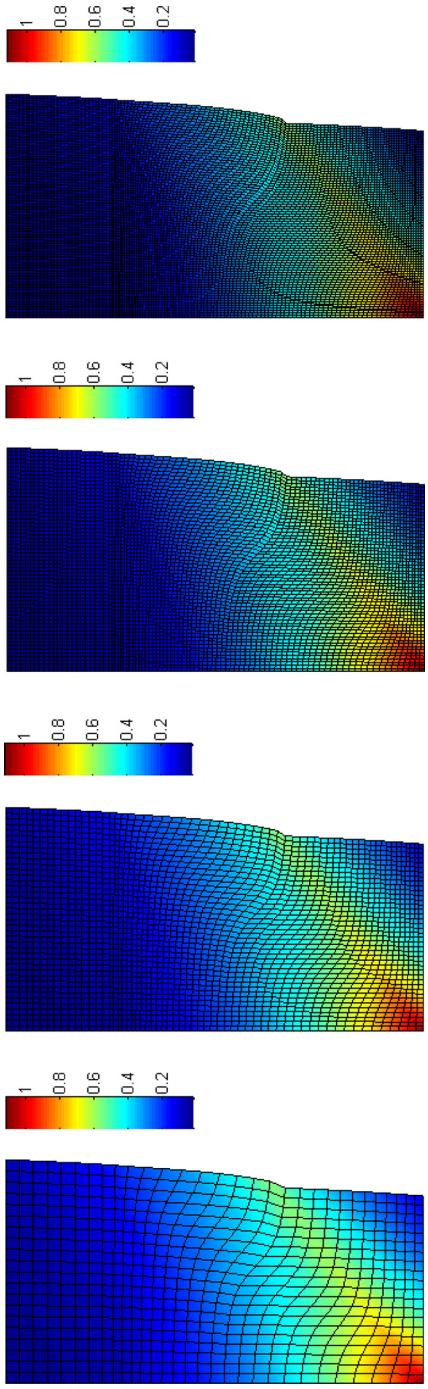

Fig. 6. Contours of equivalent plastic strain under plane strain tension II on four different meshes (from left to right). The length parameter is fixed at $\ell = 0.5$ mm.

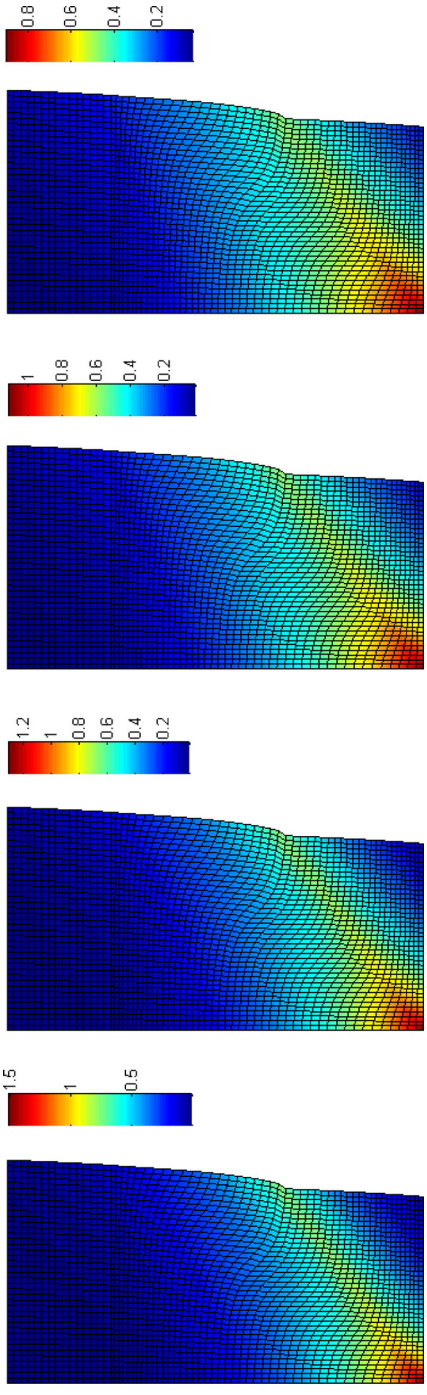

Fig. 7. Contours of equivalent plastic strain under plane strain tension II with four different values of the length parameter $\ell = 0.3$ mm, $\ell = 0.4$ mm, $\ell = 0.5$ mm and $\ell = 0.6$ mm on a fixed mesh (from left to right).

and (ii) regularized parameter sensitivity. For the first problem, we construct three meshes with $30 \times 20 = 600$, $60 \times 40 = 2400$, $90 \times 60 = 5400$ and $120 \times 80 = 9600$ finite elements, and study shear localization on different meshes. For the second problem, we change the values of the regularized parameter ℓ on the same finite element mesh.

Second, the collapse of the thick-walled cylinders (TWC) is simulated. We demonstrate the performance of the proposed phase model formulation for capturing the spontaneous multiple ASBing in the collapsing SS304L cylinder. The outer and inner copper shells are computed by the isotropic J_2-plasticity model. Simulation results are compared with that of both explosively and electro-magnetically driven experiments (Lovinger et al., 2011; 2015; Nesterenko and Bondar, 1994). The distribution and evolution of the multiple adiabatic shear bands are in good agreement with experimental evidences.

4.1. Plane tension tests

The boundary conditions for tension test I and II are listed in a table (as shown in Fig. 2): u denotes the displacement, T denotes the tension, and a is a non-zero value. The index 1 and 2 means in x-direction and in y-direction, respectively. For tension test I, the edges BC and AD are taken to be traction-free. For tension test II, the edge BC is taken to be traction-free. Under tension condition I the corresponding contours of the equivalent plastic strain $\boldsymbol{\varepsilon}_p$ at $a = 2.0mm$ are shown in Fig. 3. Note that no geometrical or loading asymmetries were introduced to trigger shear localizations. Over three computational meshes from coarse to fine, the shear bands are nearly the same to each other and converge with the mesh refinement. There is no significant mesh dependency in the simulation results of our phase field formulation. To observe the effects of the regularized length parameter ℓ on the width of an ASB, we change the values of ℓ to $0.3mm$, $0.4mm$, $0.5mm$ and $0.6mm$ on a fixed mesh. The contours of $\boldsymbol{\varepsilon}_p$ at $a = 2.0mm$ are displayed in Fig. 4.

Edge	Tension test I	Tension test II
DA	$T_1 = 0,\ T_2 = 0$	$u_1 = 0,\ T_2 = 0$
AB	$u_1 = 0,\ u_2 = 0$	$u_2 = 0,\ T_1 = 0$
BC	$T_1 = 0,\ T_2 = 0$	$T_1 = 0,\ T_2 = 0$
CD	$u_1 = 0,\ u_2 = a$	$u_2 = a,\ T_1 = 0$

Under tension condition II the corresponding contours of the equivalent plastic strain $\boldsymbol{\varepsilon}_p$ at $a = 2.0mm$ are shown in Fig. 6. Over three computational meshes from coarse to fine, the shear bands are nearly the same to each other and converge with the mesh refinement. There is no significant mesh dependency in the simulation results of our phase field formulation. To observe the effects of the regularized length parameter ℓ on the width of an ASB, we change the values of ℓ to $0.3mm$, $0.4mm$ and $0.5mm$ on a fixed mesh. The contours of $\boldsymbol{\varepsilon}_p$ at $a = 2.0$ mm are displayed in Fig. 7.

The force-displacement curves under plane strain tension I and II are displayed in Figs. 5 and 8, respectively. They exhibit little mesh dependency: for different mesh sizes the profiles of the force-displacement curves are similar to each other and converge with mesh refinement. The widths of the shear bands are finite and independent of the computational meshes (observed from the left of Figs. 5 and 8). For five different values of ℓ, the force-displacement curves show that the force decreases at a slower rate as ℓ increases. Meanwhile, the width of the shear bands increases (the shear bands are more diffused) and the maximum equivalent plastic strain inside the shear bands decreases (observed from the right of Figs. 5 and 8).

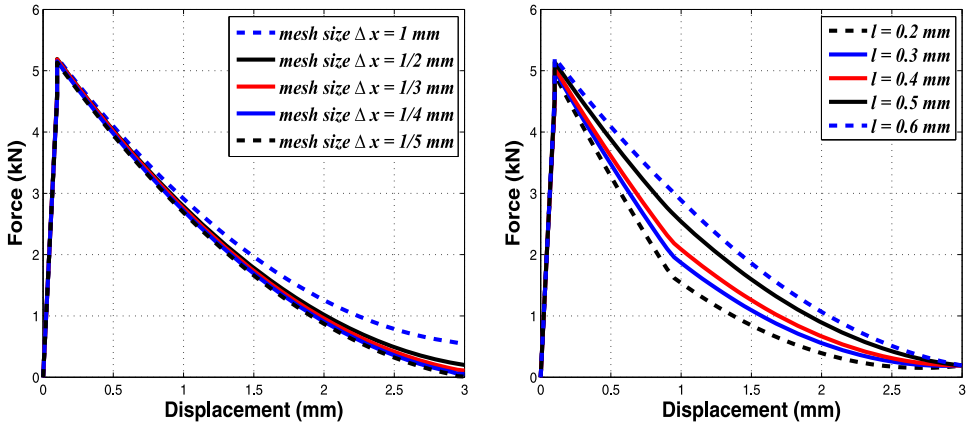

Fig. 8. Force versus displacement curves under plane strain tension II. Left: for different computational mesh sizes; Right: for different ℓ values.

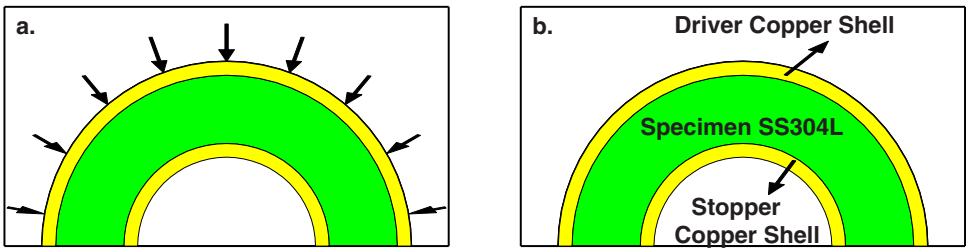

Fig. 9. Model setup. (a) The model consists of three sandwiched cylinders Cu-SS-Cu, and the loading condition is exerted on the outer copper shell. (b) The phase field model is used for SS (in green), and J_2-plasticity is adopted for Cu (in yellow). (For interpretation of the references to colour in this figure legend, the reader is referred to the web version of this article.)

4.2. TWC test

The thick-walled SS304L cylinder is sandwiched between two cylindrical copper shells, and the shells are driven inwards, as shown in Fig. 9. Specimen symmetry and plain strain conditions are used in this simulation. The boundary velocities are loaded on the outer copper shell, and the duration time is $5.0\mu s$. The diameter of the outer copper cylinder, the SS specimen and the inner copper cylinder are $5.0 - 5.4\,\text{mm}$, $3.0 - 5.0\,\text{mm}$ and $2.6 - 3.0\,\text{mm}$, respectively. The parameters of SS304L are taken from Meyers et al. (2001), and the isotropic J2-plasticity material parameters for copper can be found in Lovinger et al. (2011).

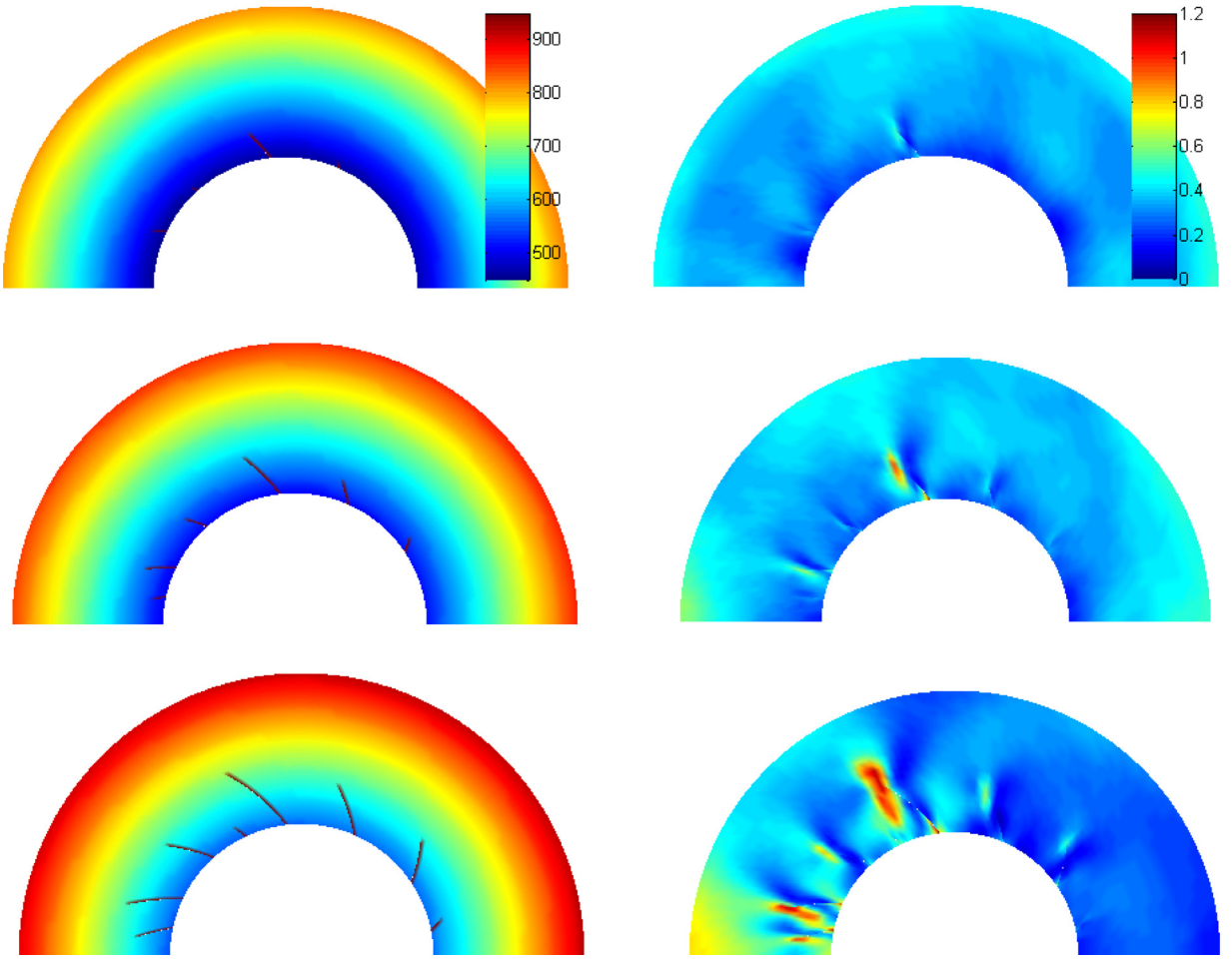

Fig. 10. Simulation results for loading velocity $v = 100\,\text{m}\cdot\text{s}^{-1}$ at $t = 15\,\mu s$, $t = 20\mu s$ and $t = 25\mu s$ (from top to bottom): contours of the temperature distribution (the left column, unit: K), and the von Mises stress distribution (the right column, unit: GPa).

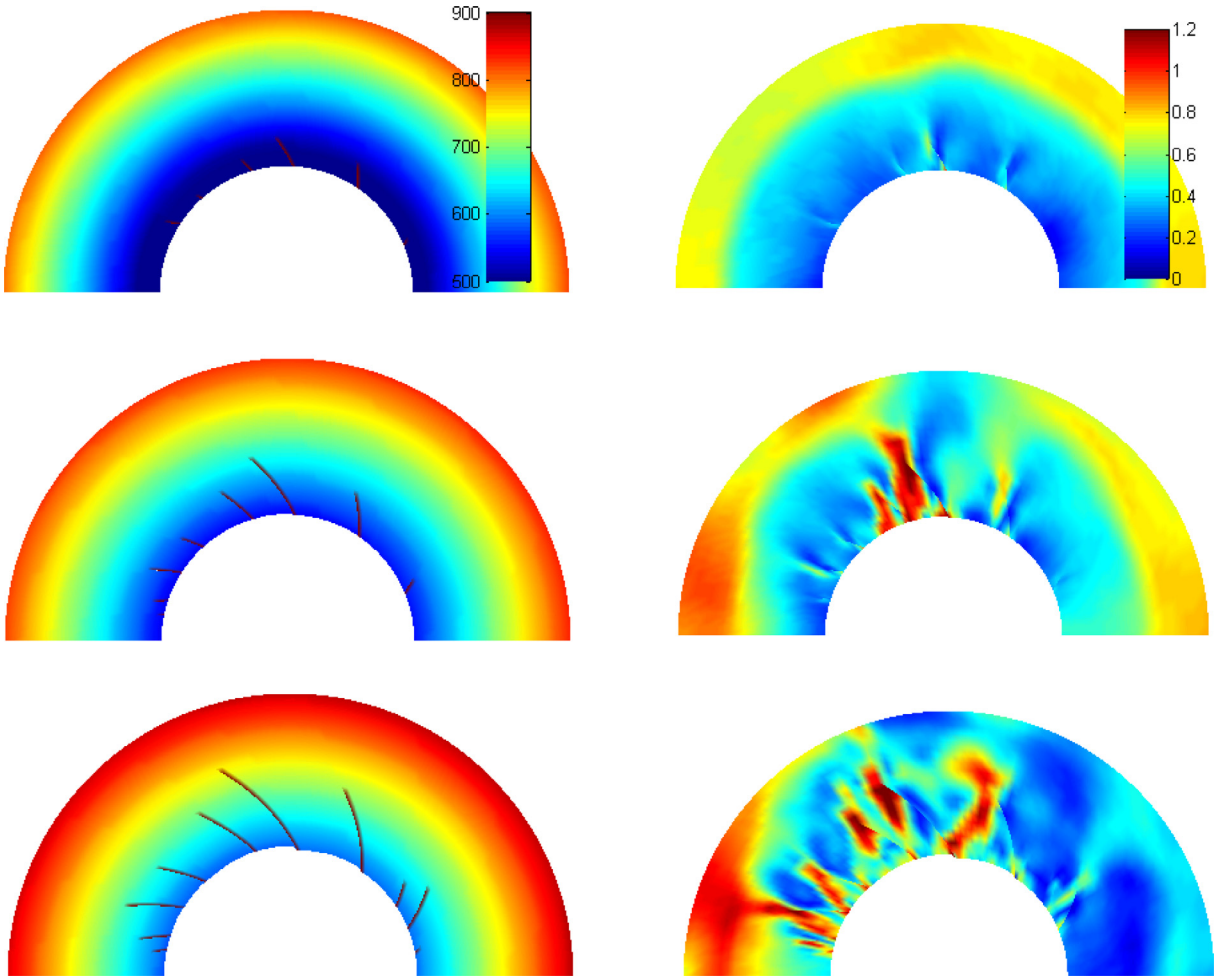

Fig. 11. Simulation results for loading velocity $v = 150\,\mathrm{m}\cdot\mathrm{s}^{-1}$ at $t = 15\mu s$, $t = 20\mu s$ and $t = 25\mu s$ (from top to bottom): contours of the temperature distribution (the left column, unit: K), and the von Mises stress distribution (the right column, unit: GPa).

Numerical perturbation is a commonly used simulation strategy for investigating spontaneous multiple shear localization (Liu et al., 2016; Lovinger et al., 2011; Zhou et al., 2006). Experimental observations showed that the grains inside the work-hardened layer had a special orientation along the cutting direction and all the shear bands displayed a single direction spiral pattern (Xue et al., 2003). The single direction spiral perturbation has been applied to trigger the initiation and formation of shear bands in the TWCs, which results in counter-clockwise propagated multiple shear bands. The size of the perturbation region is assumed to be several elements in $\pi/4$ tangential direction along the inner surface of the TWC specimen, inside which the local yield stresses are softened to be 80% of their initial values (Liu et al., 2016). Since each position at the inner surface has the same chance to trigger a shear band, the locations of the perturbation regions are calculated from a random number generator, and hence are varied for different simulations. The number of the shear bands is determined by the random number generator. It is calibrated by experimental observations under different loading conditions. In the initiation and early stage, mesh size has no influence to the number of the shear bands. With further propagation and strain localization, more complex structures such as bifurcation and interaction between shear bands are resolved better on finer computational meshes.

Time evolutions of the temperature and the von Mises stress distribution for loading velocities $v_1 = 100\,\mathrm{ms}^{-1}$ and $v_2 = 150\,\mathrm{ms}^{-1}$ are displayed in Figs. 10 and 11. We take the critical shear banding energy density $\mathcal{G}_A = 2.15 \times 10^3 \mathrm{J}\cdot\mathrm{m}^{-2}$ as the initiation criterion of ASBs, and find that the multiple shear bands are initiated on the internal surface of the SS cylindrical specimen. The general observations are in good agreement with that of experiments (Lovinger et al., 2011; Meyers et al., 2001). The von Mises stress concentrates at the band tips, and decreases quickly as the ASBs propagate ahead. For larger loading velocity, higher temperature and stress peak are reached, which promote the occurrence of shear localization and failure.

The characteristics of multiple shear bands pattern are illustrated in Fig. 12(A). Simulation results show that the proposed phase field model can predict the spontaneous shear instability and strain localization. Fig. 12(B) demonstrates profiles of

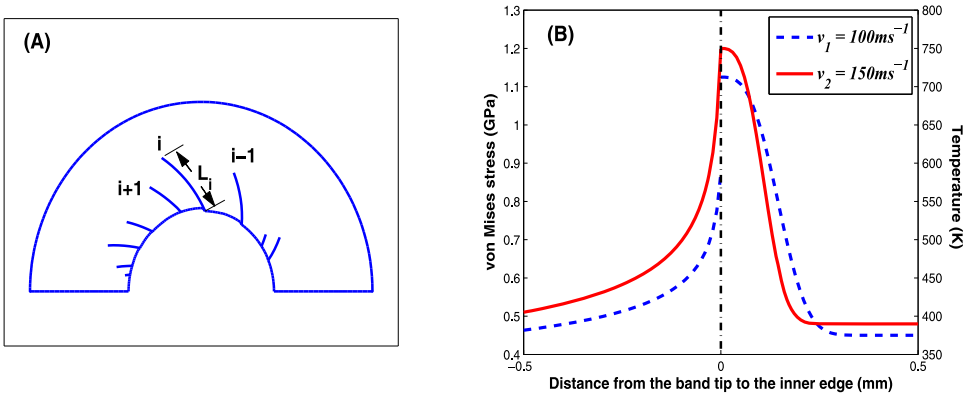

Fig. 12. Shear band length distribution. (A) Characteristics of shear band pattern: L_i is the length of the ith shear band. (B) The distributions of von Mises stresses and temperatures from the shear band tip to the internal surface. (For interpretation of the references to color in this figure, the reader is referred to the web version of this article.)

the von Mises stress and the temperature of spontaneous multiple ASBs in the collapsing cylinder. The x-axis denotes the distance from the shear band tip to the internal surface in radial direction. Results for loading velocity $v_1 = 100\,\mathrm{ms}^{-1}$ are expressed by black dash lines, and for $v_2 = 150\,\mathrm{ms}^{-1}$ are expressed by red solid lines. The stress value for v_2 achieves 1.2 GPa at the band tip, and decreases fast to 0.51 GPa at the radial location with the distance of 0.5 mm. For v_1 the stress changes from 0.85 GPa to 0.47 GPa. It means that the stress has been released after the propagation of ASBs. The temperatures decay with a kernel structure. The maximum temperature for v_2 is 750 K at the band tip, and slowly downto about 700 K, then quickly decay to about 400 K at the radial location with the distance of 0.15 mm. Similar tendency of temperature for v_1 can be observed, revealing the strongly dependence of ASBs on the rapid rise of temperatures.

5. Summary and conclusions

The theoretical and computational framework of a general phase field formulation for simulating ASBs is given and discussed. It provides a new tool to explore the essential mechanism that stems from micro-structural plasticity for the initiation of ASB under dynamic conditions. The phase field length scale ℓ to some extent is a regularization parameter defines the width of the diffuse shear band process zone. It is used to model the post-initiation stage of localization of plastic deformation in shear bands of finite thickness. Future studies will focus on determination of more physically reasonable values for the phase field length scale ℓ. It is different from the strain gradient plasticity length scale, which has physical grounds including dislocation motion and strain hardening from experimental evidences, with a value on the order of microns. However, they have one thing in common: they can regularize strain softening behavior so as to avoid mesh-dependency related issues during numerical simulations, and the obtained shear band widths are dependent on the values of them. The following points are concluded:

1. The proposed phase field framework works well for simulating the initiation and propagation of ASBs in elastic-plastic solids. In the phase field formulation, the derivation of shear banding energy density and the Griffith's regularized ASB surface energy approximation proved to be an effective way to characterize the energy dissipation in ASBing, which is closely related to the underlying physical mechanisms of ASBs.
2. Using energy minimization and ASB canonical structural analysis, we find that ASB phase field formulation reduces to a standard strain-gradient plasticity model. The rescaled ASB surface density function in the phase field formulation and the gradient enhanced plastic strain rate in conventional strain-gradient models have exactly the same expressions, by which the hardening modulus and work-conjugate stress of the corresponding strain-gradient model can be obtained explicitly.
3. This relationship bridges the two established theories, and deepens the understanding of energy dissipation, shear instability and size effects for the dynamic localization in propagating ASBs. For example, as a reason to the good performances for problems involving strain-softening, this phase field formulation has implicitly incorporated the strain-gradient regularization by the characteristic length scale.
4. The constitutive relations are calculated in a coupled way from the evolution of phase field equation and atomistic potentials consistent hyperelastic-plasticity. Based on system energy decomposition, the degraded volumetric strain energy is applied to calculate the elastic responses. The degraded deviatoric strain energy and the surface energy of ASB are used to account for the combined effects of dynamic localization, plasticity and fracture, which directly relates energy dissipation to the evolution of dynamic ASBs.
5. Numerical experiments are carried out to show the accuracy and efficiency of our phase field formulation. The plane tension tests displayed that the strain-softening in ASBs can be captured without pathological mesh-dependence. The

regularized parameter controls the widths of ASBs, which is equivalent to that of the characteristic length scale appeared in strain-gradient plasticity theories. The advantage in capturing discontinuous surfaces is demonstrated by the collapse of thick-walled cylinders. The distribution and evolution of the multiple ASBs are in good agreement with the experimental evidences.

Declaration of Competing Interest

We declare that we have no financial and personal relationships with other people or organizations that can inappropriately influence our work, there is no professional or other personal interest of any nature or kind in any product, service and/or company that could be construed as influencing the position presented in, or the review of, the manuscript entitled 'A phase field framework for dynamic adiabatic shear banding' by Yun Xu, Pingbing Ming and Jun Chen.

CRediT authorship contribution statement

Yun Xu: Methodology, Writing - original draft, Software. **Pingbing Ming:** Methodology, Writing - review & editing. **Jun Chen:** Conceptualization, Writing - review & editing.

Acknowledgements

In this research Y. Xu is supported by National Natural Science Foundation of China Grant no. 11772067 and CAEP Foundation of China Grant no. CX2019032, P.B. Ming is supported by National Natural Science Foundation of China Grant no. 11971467 and Distinguished Young Scholars no. 11425106, and J. Chen is supported by National Natural Science Foundation of China Grant no. 11572053.

References

Ambati, M., Gerasimov, T., Lorenzis, L., 2015. Phase-field modeling of ductile fracture. Comput. Mech. 55, 1017–1040.
Anand, L., Aslan, O., Chester, S., 2012. A large-deformation gradient theory for elastic plastic materials: strain softening and regularization of shear bands. Int. J. Plast. 30–31, 116–143.
Arriaga, M., Waisman, H., 2017. Combined stability analysis of phase-field dynamic fracture and shear band localization. Int. J. Plast. 96, 81–119.
Bai, Y., Dodd, B., 1992. Adiabatic Shear Localization. Pergamon, Oxford.
Born, M., Huang, K., 1954. Dynamical Theory of Crystal Lattices. Oxford University Press.
Bourdin, B., Francfort, G., Marigo, J.-J., 2000. Numerical experiments in revisited brittle fracture. J. Mech. Phys. Solids 48, 797–826.
Brepols, T., Wulfinghoff, S., Reese, S., 2017. Gradient-extended two-surface damage-plasticity: micromorphic formulation and numerical aspects. Int. J. Plast. 97, 64–106.
Daw, M., Baskes, M., 1984. Embedded-atom method – derivation and application to impurities, surfaces, and other defects in metals. Phys. Rev. B 29, 6443–6453.
Dolinski, M., Rittel, D., 2015. Experiments and modeling of ballistic penetration using an energy failure criterion. J. Mech. Phys. Solids 83, 1–18.
Dolinski, M., Rittel, D., Dorogoy, A., 2010. Modeling adiabatic shear failure from energy considerations. J. Mech. Phys. Solids 58, 1759–1775.
Duda, F., Ciarbonetti, A., Sánchez, P., Huespe, A., 2015. A phase-field/gradient damage model for brittle fracture in elastic–plastic solids. Int. J. Plast. 65, 269–296.
E, W., Ming, P., 2007. Cauchy-born rule and the stability of crystalline solids: static problems. Arch. Ration. Mech. Anal. 183(2), 241–297.
Fleck, N., Hutchinson, J., 2001. A reformulation of strain gradient plasticity. J. Mech. Phys. Solids 49, 2245–2271.
Fleck, N., Willis, J., 2009. A mathematical basis for strain gradient plasticity theory. Part I: scalar plastic multiplier. J. Mech. Phys. Solids 57, 161–177.
Francfort, G., Marigo, J.-J., 1998. Revisiting brittle fracture as an energy minimization problem. J. Mech. Phys. Solids 46(8), 1319–1342.
Giambanco, G., Ribolla, E., 2019. A phase-field model for strain localization analysis in softening elastoplastic materials. Int. J. Solids Struct. 172–173, 84–96.
Glimm, J., Plohr, B., Sharp, D., 1993. A conservative formulation for large-deformation plasticity. Appl. Mech. Rev. 46, 519–526.
Grady, D., 1994. Dissipation in adiabatic shear bands. Mech. Mater. 17, 289–293.
Gudmundson, P., 2004. Unified treatment of strain gradient plasticity. J. Mech. Phys. Solids 52, 1379–1406.
Hutchinson, J., 2012. Generalizing J_2 flow theory: fundamental issues in strain gradient plasticity. Acta Mech. Sin. 28, 1078–1086.
LeSar, R., Najafabadi, R., Srolovitz, D., 1989. Finite-temperature defect properties from free-energy minimization. Phys. Rev. Lett. 63, 624.
Liu, M., Guo, Z., Fan, C., Tang, T., Wang, X., Hu, H., 2016. Modeling spontaneous shear bands evolution in thick-walled cylinders subjected to external high-strain-rate loading. Int. J. Solids Struct. 97–98, 336–354.
Loew, P., Peters, B., Beex, L., 2019. Rate-dependent phase-field damage modeling of rubber and its experimental parameter identification. J. Mech. Phys. Solids 127, 266–294.
Lovinger, Z., Rikanati, A., Rosenberg, Z., Rittel, D., 2011. Electro-magnetic collapse of thick-walled cylinders to investigate spontaneous shear localization. Int. J. Impact Eng. 38, 918–929.
Lovinger, Z., Rittel, D., Rosenberg, Z., 2015. An experimental study on spontaneous adiabatic shear band formation in electro-magnetically collapsing cylinders. J. Mech. Phys. Solids 79, 134–156.
Martinez-Paneda, E., Golahmar, A., Niordson, C., 2018. A phase field formulation for hydrogen assisted cracking. Comput. Methods Appl. Mech. Eng. 342, 742–761.
McAuliffe, C., 2014. Numerical Modeling of Shear Bands and Dynamic Fracture in Metals (PhD thesis). Columbia University.
McAuliffe, C., Waisman, H., 2015. A unified model for metal failure capturing shear banding and fracture. Int. J. Plast. 65, 131–151.
Meyers, M., Nesterenko, V., LaSalvia, J., Xue, Q., 2001. Shear localization in dynamic deformation of materials: microstructural evolution and self-organization. Mater. Sci. Eng. A 317, 204–225.
Miehe, C., 2011. A multi-field incremental variational framework for gradient-extended standard dissipative solids. J. Mech. Phys. Solids 59, 898–923.
Miehe, C., Teichtmeister, S., Aldakheel, F., 2016. Phase-field modelling of ductile fracture: a variational gradient-extended plasticity-damage theory and its micromorphic regularization. Philos. Trans. R. Soc. A 374, 20150170.
Nesterenko, V., Bondar, M., 1994. Localization of deformation in collapse of a thick walled cylinder. Combust. Explos. Shock Waves 30(4), 500–505.
Olmstead, W., 1994. Shear bands as surfaces of discontinuity. J. Mech. Phys. Solids 42(4), 697–709.
Simo, J., 1988. A framework for finite strain elastoplasticity based on maximum plastic dissipation and the multiplicative decomposition: part I. Continuum formulation. Comput. Meth. Appl. Mech. Eng. 66, 199–219.

Simo, J., Hughes, T., 1998. Computational Inelasticity. Springer.
Tanne, E., Li, T., Bourdin, B., Marigo, J.-J., Maurini, C., 2018. Crack nucleation in variational phase-field models of brittle fracture. J. Mech. Phys. Solids 110, 80–99.
Tvergaard, V., Needleman, A., 1995. Effects of nonlocal damage in porous plastic solids. Int. J. Solids Struct. 32(8–9), 1063–1077.
Wright, T., 2002. The Physics and Mathematics of Adiabatic Shear Bands. Cambridge University Press, Cambridge.
Wright, T., Ravichandran, G., 1997. Canonical aspects of adiabatic shear bands. Int. J. Plasticity 13(4), 309–325.
Wright, T., Walter, J., 1996. The asymptotic structure of an adiabatic shear band in antiplane motion. J. Mech. Phys. Solids 44, 77–97.
Xu, Y., Chen, J., 2015. Atomistic potentials based energy flux integral criterion for dynamic adiabatic shear banding. J. Mech. Phys. Solids 75, 45–57.
Xu, Y., Chen, J., Li, H., 2014. Finite hyperelastic–plastic constitutive equations for atomistic simulation of dynamic ductile fracture. Int. J. Plast. 59, 15–29.
Xue, Q., Nesterenko, V., Meyers, M., 2003. Evaluation of the collapsing thick-walled cylinder technique for shear-band spacing. Int. J. Impact Eng. 28(3), 257–280.
Zener, C., Hollomon, J., 1944. Effect of strain rate upon plastic flow of steel. J. Appl. Phys. 15(1), 22–32.
Zhou, F., Wright, T., Ramesh, K., 2006. The formation of multiple adiabatic shear bands. J. Mech. Phys. Solids 54(7), 1376–1400.
Zhou, M., Rosakis, A., Ravichandran, G., 1998. On the growth of shear bands and failure- mode transition in prenotched plates: a comparison of singly and doubly notched specimens. Int. J. Plasticity 14(4–5), 435–451.